Space Sci Rev (2017) 211:547–570
DOI 10.1007/s11214-016-0324-6

Finite-Difference Modeling of Acoustic and Gravity Wave Propagation in Mars Atmosphere: Application to Infrasounds Emitted by Meteor Impacts

Raphael F. Garcia[1,2] · Quentin Brissaud[1] · Lucie Rolland[3] · Roland Martin[4] · Dimitri Komatitsch[5] · Aymeric Spiga[6] · Philippe Lognonné[7] · Bruce Banerdt[8]

Received: 8 June 2016 / Accepted: 24 November 2016 / Published online: 12 December 2016

Abstract The propagation of acoustic and gravity waves in planetary atmospheres is strongly dependent on both wind conditions and attenuation properties. This study presents a finite-difference modeling tool tailored for acoustic-gravity wave applications that takes into account the effect of background winds, attenuation phenomena (including relaxation effects specific to carbon dioxide atmospheres) and wave amplification by exponential density decrease with height. The simulation tool is implemented in 2D Cartesian coordinates and first validated by comparison with analytical solutions for benchmark problems. It is then applied to surface explosions simulating meteor impacts on Mars in various Martian atmospheric conditions inferred from global climate models. The acoustic wave travel times are validated by comparison with 2D ray tracing in a windy atmosphere. Our simulations predict that acoustic waves generated by impacts can refract back to the surface on wind ducts at high altitude. In addition, due to the strong nighttime near-surface temperature gradient on Mars, the acoustic waves are trapped in a waveguide close to the surface, which allows a night-side detection of impacts at large distances in Mars plains. Such theoretical

✉ R.F. Garcia
Raphael.Garcia@isae.fr

1 Institut Supérieur de l'Aéronautique et de l'Espace (ISAE-SUPAERO), Université de Toulouse, 10 Ave E. Belin 31400 Toulouse, France

2 Institut de Recherche en Astrophysique et Planétologie, Université de Toulouse, 14 Ave E. Belin, 31400 Toulouse, France

3 Université Côte d'Azur, Observatoire de la Côte d'Azur, Géoazur UMR 7329, CNRS, 250 rue Albert Einstein, Sophia Antipolis, 06560 Valbonne, France

4 Laboratoire de Géosciences Environnement Toulouse GET, UMR CNRS 5563, Observatoire Midi-Pyrénées, Université Paul Sabatier, 14 avenue Édouard Belin, 31400 Toulouse, France

5 LMA, CNRS UPR 7051, Aix-Marseille University, Centrale Marseille, Marseille, France

6 Laboratoire de Météorologie Dynamique, UMR CNRS 8539, Institut Pierre-Simon Laplace, Sorbonne Universités, UPMC Univ Paris 06, 4 place Jussieu, 75005 Paris, France

7 Institut de Physique du Globe de Paris, Sorbonne Paris Cité, Université Paris Diderot, 75013 Paris, France

8 Jet Propulsion Laboratory, Pasadena, CA 91109, USA

predictions are directly applicable to future measurements by the INSIGHT NASA Discovery mission.

Keywords Mars · InSight mission · Atmosphere · Acoustic waves · Gravity waves · Impacts · Pressure sensor · Numerical modeling

1 Introduction

Measurements of pressure perturbations from infrasounds and gravity waves in the atmosphere of Mars provide a way to locate in space and time the infrasonic sources and to infer the Martian atmospheric properties from the wave propagation. The two main differences between Mars and Earth in terms of the infrasonic wave propagation are the following. First, the day-side temperature structure of Mars atmosphere is such that the sound velocity continuously decreases from the surface up to the thermosphere, preventing acoustic signals, generated at the bottom of the atmosphere, from refracting back to the surface. Second, the attenuation of acoustic waves by carbon dioxide molecular relaxation must be accounted for on Mars (Bass and Chambers 2001; Williams 2001; Petculescu and Lueptow 2007; Hanford and Long 2009). In particular, the relaxation frequency of vibrational modes of CO_2 molecules is within the acoustic-infrasonic range below 80 km of altitude. Thus the attenuation of infrasounds is higher than for the Earth. A consequence of those two differences is that Mars appears less favorable than the Earth for ground measurement of infrasonic signals coming from sources located at the surface. Yet, those effects remain to be quantified especially in the context of the INSIGHT mission that will deploy pressure and seismic sensors on the surface.

Infrasound and gravity wave propagation on Earth has been studied since the seventies (Hines 1960) but this topic regained interest recently when infrasonic and gravity waves were detected in the thermosphere (Artru et al. 2004, 2005 Liu et al. 2006; Bruinsma and Forbes 2008; Rolland et al. 2010). Simulations of acoustic and gravity wave propagation in Earth's atmosphere have been carried out by various authors (Ostashev et al. 2005; de Groot-Hedlin et al. 2011; Mikhailenko and Mikhailov 2014; Brissaud et al. 2016). But to our knowledge, numerical simulations for acoustic and gravity wave propagation in a windy martian atmosphere including vibrational relaxation have never been performed.

This study first presents a numerical method which is able to simulate acoustic and gravity wave propagation in a windy and attenuating Martian atmosphere. The numerical simulations are validated with respect to analytical solutions, and also compared to ray tracing results (Dessa et al. 2005). The method is then applied to a surface explosion in realistic Mars atmosphere models, which enables inference of the variability of wave propagation conditions with respect to Mars climate.

2 Finite-Difference Modeling of Acoustic and Gravity Waves in a Carbon Dioxide Planetary Atmosphere

2.1 Governing Equations

In this study we use the linearized Navier-Stokes equations for acoustic and gravity wave propagation in an attenuating atmosphere subject to bulk, shear and vibrational relaxation. We consider the same physical assumptions as in Brissaud et al. (2016). Only vertically

stratified atmosphere models and horizontal winds are considered. In this case, the equations are

$$\begin{aligned}\partial_t p &= -\mathbf{w}.\nabla p - \rho c^2 \nabla.\mathbf{v} - \rho \mathbf{v}.\mathbf{g} + e_1,\\ \partial_t \rho_p &= -\mathbf{w}.\nabla \rho_p - \nabla.(\rho \mathbf{v}),\\ \rho \partial_t \mathbf{v} &= -\rho\left\{(\mathbf{v}.\nabla)\mathbf{w} + (\mathbf{w}.\nabla)\mathbf{v}\right\} + \nabla.\boldsymbol{\Sigma} + \mathbf{g}\rho_p,\end{aligned} \tag{1}$$

where ρ is the background density, $\mathbf{w}$ the horizontal wind velocity, c the adiabatic sound velocity, $\mathbf{g}$ the gravity acceleration, p the pressure perturbation, $\mathbf{v}$ the velocity perturbation, ρ_p the density perturbation, e_1 a memory variable taking into account relaxation effects due to carbon dioxide vibrational relaxation (see Sect. 2.2) and $\boldsymbol{\Sigma}$ is the stress tensor, which reads

$$(\boldsymbol{\Sigma})_{ij} = -p\delta_{ij} + \mu\left(\partial_j(\mathbf{v}+\mathbf{w})_i + \partial_i(\mathbf{v}+\mathbf{w})_j - \frac{2}{3}\delta_{ij}\nabla.\mathbf{v}\right) + \eta_V \delta_{ij}\nabla.\mathbf{v}. \tag{2}$$

where (i, j) indices indicate space directions, μ is the shear viscosity and η_V the volume viscosity. Note that, due to the memory variable, equation system (1) lacks constraint and an extra equation needs to be added as explained in Sect. 2.2.3.

The system of equations (1) describes the propagation of acoustic and gravity waves in a viscous atmospheric fluid subject to wind (Nappo 2002).

2.2 Acoustic Attenuation in Mars Atmosphere

2.2.1 Analytical Formulation of Absorption Coefficients

Additional attenuation processes must be considered for Mars with respect to Earth due to the presence of CO_2. In this section, we will recall results from Bass and Chambers (2001) for the atmosphere composition as well as absorption coefficient equations. Thus, we will assume that the composition of the Martian atmosphere is 95.3 % CO_2 and, accordingly, we will include the effects of sound relaxation by vibrational and rotational modes of CO_2 molecules. On Mars, three kinds of absorption have an impact on wave propagation, and we detail here the analytical formulation of the three distinct absorption coefficients. These analytical expressions were validated by Direct Simulation Monte Carlo method (Hanford and Long 2009).

First, classical absorption, also present on Earth, due to viscosity and thermal conduction reads

$$\alpha_{cl} = \frac{\omega^2}{2\rho c^3}\left(\frac{4}{3}\mu + \frac{(\gamma-1)\kappa}{\gamma C_v}\right), \tag{3}$$

where ω in $2\pi\cdot\mathrm{s}^{-1}$ is the wave angular frequency, c in $\mathrm{m}\cdot\mathrm{s}^{-1}$ the adiabatic sound speed, μ in $\mathrm{kg}\cdot\mathrm{m}^{-1}\cdot\mathrm{s}^{-1}$ the dynamic viscosity, $\gamma = C_p/C_v$ the specific heat ratio, C_v and C_p in $\mathrm{J}\cdot\mathrm{kmol}^{-1}\cdot\mathrm{K}^{-1}$ the molar zero frequency specific heat respectively at constant volume and constant presure, and κ in $\mathrm{J}\cdot\mathrm{kmol}^{-1}\cdot\mathrm{K}^{-1}\cdot\mathrm{kg}\cdot\mathrm{m}^{-1}\cdot\mathrm{s}^{-1}$ the thermal conductivity.

The absorption process caused by rotational modes of CO_2 molecules is specific to Mars. It reads

$$\alpha_{rot} = \frac{\omega^2}{2\rho c^3}\mu\frac{\gamma(\gamma-1)R}{1.25C_p^0}Z_{rot}, \tag{4}$$

where $C_p^0 = 7/2$ in J·kmol^{-1}·K^{-1} is the specific heat at constant pressure, $R = 8.31432 \times 10^3$ in J·kmol^{-1}·K^{-1} is the gas constant and zero frequency and Z_{rot} is the rotational collision number. The above two attenuation mechanisms have a similar frequency dependence. So, the attenuation induced by rotational modes of CO_2 molecules is simply taken into account by defining the volume viscosity as:

$$\eta_V = \left(\frac{4}{3} + \frac{\gamma(\gamma-1)R}{1.25C_p^0} Z_{rot}\right)\mu + \frac{(\gamma-1)\kappa}{\gamma C_v}. \tag{5}$$

The third absorption process is the vibrational relaxation that reads, in the case of a CO_2 atmosphere

$$\alpha_{vib} = \frac{\frac{\pi S_{vib}}{c}\left(\frac{f^2}{f_r}\right)}{1 + \left(\frac{f}{f_r}\right)^2}, \tag{6}$$

where

$$S_{vib} = C_j' \frac{R}{C_p^\infty (C_v^\infty + C_j')} \quad \text{(Relaxation strength)},$$

$$f_r = \frac{1}{2\pi \tau_{vs}'} \quad \text{(Relaxation frequency)}$$

with τ_{vs}' being the relaxation time at constant volume and temperature for a single energy-transfer reaction, it determines the rate of the relaxation process. The smaller the relaxation time, the faster the relaxation process. C_p^∞ in J·kmol^{-1}·K^{-1} is the constant pressure specific heat at frequencies well above the relaxation frequency f_r in Hz, C_p^0 its value well below f_r and C_j' in J·kmol^{-1}·K^{-1} is the specific heat of the relaxing mode.

Figure 1, shows that below 80 km altitude on Mars the main attenuation factor comes from the CO_2 vibrational relaxation. Thus, taking this effect into account in simulations is crucial to correctly model infrasound propagation. Also, as one notices in Fig. 1, the vibrational absorption coefficient does not follow the trend of classical and rotational absorption, presenting a peak relaxation frequency. Consequently, this attenuation process must be analytically and numerically integrated into the equations in a different way than classical and rotational absorptions. In the next section, we demonstrate that the Zener rheology model (Carcione et al. 1988) is equivalent to the attenuation mechanism induced by CO_2 vibrational modes. Then, the Zener relaxation times are used to define a memory variable that will numerically model the CO_2 vibrational relaxation process.

2.2.2 A Zener Model for Carbon Dioxide Vibrational Relaxation

We demonstrate in this section that the vibrational absorption coefficient in (6) is equivalent to the one induced by a Zener attenuation mechanism (Carcione 2007, Sect. 2.4.3). In that book further details can be found about the Zener rheology and we will thus only present the relationship between the absorption coefficient induced by a Zener attenuation mechanism and the analytical one from (6).

The quality factor, for a Zener linear solid, reads (Carcione 2007, Eq. (2.159))

$$Q(\omega) = \frac{1 + \omega^2 \tau_\epsilon \tau_\sigma}{\omega(\tau_\epsilon - \tau_\sigma)}, \tag{7}$$

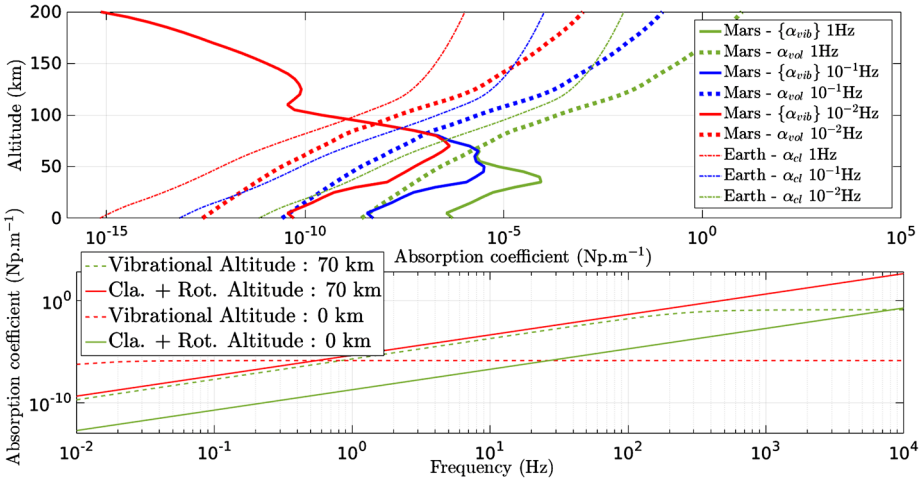

Fig. 1 On *top*, vibrational absorption coefficient from (6) $\{\alpha_{vib}\}$ and the sum between volume absorption coefficients (which is the sum of classical and rotational relaxations $\alpha_{vol} = \alpha_{cl} + \alpha_{rot}$) from (3)–(4) against altitude on Mars at various frequencies $f = 10^{-2}, 10^{-1}, 1$ Hz; and classical absorption coefficients against altitude on Earth $\{\alpha_{cl}\}$ at same frequencies. On the *bottom*, sum of the classical and rotational absorption coefficients; and vibrational absorption coefficient, presented in the range $(10^{-2}$–$10^{4})$ Hz at various altitudes $z = 0, 70$ km

where τ_ϵ and τ_σ are, respectively, strain and stress relaxation times. The time τ_σ characterizes the time during which stress decreases by a characteristic value and the terminology strain relaxation time τ_ϵ, also called retardation time, comes from the exponential dependence of the creep function (refer to Carcione 2007). Considering a low-viscosity approximation ($Q \gg 1$), the approximate coefficient can be written as (Carcione 2007, Eq. (2.123))

$$\alpha \approx \frac{\omega}{2c} Q^{-1}. \tag{8}$$

Thus, from (7)–(8), one can establish a relationship between the analytical and Zener absorption coefficients

$$\alpha \approx \frac{\omega}{2c} Q^{-1} = \frac{1}{2c} \frac{\omega^2(\tau_\epsilon - \tau_\sigma)}{1 + \omega^2 \tau_\epsilon \tau_\sigma} = \frac{(\tau_\epsilon - \tau_\sigma)}{2c\sqrt{\tau_\epsilon \tau_\sigma}} \frac{\omega^2 \sqrt{\tau_\epsilon \tau_\sigma}}{1 + \omega^2 \tau_\epsilon \tau_\sigma} = \frac{\frac{\pi S_{vib}}{c} (\frac{f^2}{f_r})}{1 + (\frac{f}{f_r})^2} = \alpha_{vib}, \tag{9}$$

where one can identify relaxation times $\tau_\epsilon, \tau_\sigma$ with relaxation frequencies f_r and relaxation strengths S_{vib} using (6) as

$$f_r = \frac{1}{2\pi \tau_r} \quad \text{and} \quad S_{vib} = \frac{(\tau_\epsilon - \tau_\sigma)}{\tau_r}, \tag{10}$$

where $\tau_r = \sqrt{\tau_\epsilon \tau_\sigma}$. Since atmospheric models will provide relaxation frequencies and relaxation strengths, the remaining task in order to model the attenuation process consists in finding relaxation times in terms of those variables. From (10), one needs to solve a second-order ordinary differential equation, which finally gives

$$\tau_\sigma = \frac{1}{2}\left(-\frac{S_{vib}}{2\pi f_r} + \sqrt{\left(\frac{S_{vib}}{2\pi f_r}\right)^2 + \frac{4}{(2\pi f_r)^2}} \right); \qquad \tau_\epsilon = \tau_\sigma + \frac{S_{vib}}{2\pi f_r}. \tag{11}$$

2.2.3 Memory Variables for Carbon Dioxide Vibrational Relaxation Processes

In order to integrate numerically the CO_2 vibrational relaxation, we use the concept of memory variables. The general form of stress-strain relation is from Eq. (2.9) in Carcione (2007)

$$\Sigma(\mathbf{x}, t) = \Psi(\mathbf{x}, t) * \partial_t \epsilon(\mathbf{x}, t), \tag{12}$$

where $*$ is the convolution product, Σ the stress tensor (as in (2)), Ψ the relaxation tensor (scalars in 1D) and ϵ the strain.

The convolution kernel in the stress-strain relation (12) is difficult to implement in the linearized Navier-Stokes equations in time-domain methods. In this paper we will use a standard method (Carcione 2007) that consists in computing memory kernels based on a chain of linearly coupled memory variables whose frequencies correspond to moments of the memory kernel spectrum. To justify the introduction of memory variables we should go back to the main constitutive equations. In order to compute the time derivative of the convolution product in (12), we first recall the Boltzmann operation, that reads for any function g and f of the Heaviside type (meaning that $\forall t > 0$, $f(t) = \tilde{f} H(t)$ where H is the Heaviside function)

$$f \odot g = \partial_t (f * g) = f(0) g + (\partial_t \tilde{f} H) * g. \tag{13}$$

Then, applying this operation to (12) and considering Ψ to be of the Heaviside type (i.e. $\forall t > 0, \Psi(t) = \tilde{\Psi} H(t)$), one gets

$$\Sigma = \Psi * \partial_t \epsilon = \partial_t \Psi * \epsilon = \partial_t (\Psi * \epsilon) = \Psi(0) \left(\epsilon + \frac{\partial_t \tilde{\Psi} H}{\Psi(0)} * \epsilon \right) = \Psi(0)(\epsilon + \phi * \epsilon), \tag{14}$$

where the response function ϕ reads

$$\phi = \tilde{\phi} H; \quad \tilde{\phi} = \frac{\partial_t \tilde{\Psi}}{\Psi(0)}. \tag{15}$$

In the case of a Zener model one has from Eq. (2.231) in Carcione (2007)

$$\tilde{\phi} = \frac{1}{\tau_\epsilon} \left(1 - \frac{\tau_\epsilon}{\tau_\sigma} \right) e^{-\frac{t}{\tau_\sigma}}, \tag{16}$$

where τ_ϵ and τ_σ are relaxation times. Then we define the strain memory variable e_1 as

$$e_1 = \phi * \epsilon. \tag{17}$$

We apply again the Boltzmann operation to the time derivative of (17) and combining with the response function (16) we obtain a first-order differential equation in time

$$\partial_t e_1 = \phi(0)\epsilon - \frac{\epsilon}{\tau_\sigma} = -\frac{1}{\tau_\sigma} \left[\left(1 - \frac{\tau_\sigma}{\tau_\epsilon} \right) \epsilon + e_1 \right]. \tag{18}$$

Thus, the introduction of a Zener solid mechanism adds a first order in time equation to solve. The final equation system is

$$\begin{aligned}
\partial_t p &= -\mathbf{w}.\nabla p - \rho c^2 \nabla.\mathbf{v} - \rho \mathbf{v}.\mathbf{g} + e_1, \\
\partial_t \rho_p &= -\mathbf{w}.\nabla \rho_p - \nabla.(\rho \mathbf{v}), \\
\rho \partial_t \mathbf{v} &= -\rho\big\{(\mathbf{v}.\nabla)\mathbf{w} + (\mathbf{w}.\nabla)\mathbf{v}\big\} + \nabla.\boldsymbol{\Sigma} + \mathbf{g}\rho_p, \\
\partial_t e_1 &= -\frac{1}{\tau_\sigma}\left[\left(1 - \frac{\tau_\sigma}{\tau_\epsilon}\right)\nabla.\mathbf{v} + e_1\right]
\end{aligned} \tag{19}$$

with

$$(\boldsymbol{\Sigma})_{ij} = -p\delta_{ij} + \mu\left(\partial_j(\mathbf{v}+\mathbf{w})_i + \partial_i(\mathbf{v}+\mathbf{w})_j - \frac{2}{3}\delta_{ij}\nabla.\mathbf{v}\right) + \eta_V \delta_{ij}\nabla.\mathbf{v}.$$

3 Numerical Implementation

Time discretization is based on a fourth-order Runge-Kutta scheme and spatial discretization is based on a fourth-order staggered finite-difference scheme coupled with an upwind scheme for advective terms. The method is the same as in Brissaud et al. (2016) and we refer to that paper for more details.

We perform simulations in a 2D vertical Cartesian mesh in which $\Delta x = \Delta z$. We use a point source within the domain and consider a rigid boundary condition along the bottom edge of the grid, which imposes zero vertical and horizontal velocity (Brissaud et al. 2016). The only variable imposed at the boundary is the vertical velocity while pressure p and density perturbation ρ_p are not constrained. In order to enforce boundary conditions, the method of images, described for instance by Wilson and Liu (2004), is relevant to our equations (Appendix 3).

To absorb outgoing waves in an efficient way we use an absorbing boundary layer called ADE-PML (Auxiliary Differential Equation Perfectly Matched Layer) (Martin et al. 2010) at the fictitious outer edges of the mesh. We adapted it to media subject to gravity (Appendix 2).

Since we often perform simulations over a large number of grid points we resort to parallel computing implemented using the Message-Passing Interface (MPI) libraries (Gropp et al. 1994), decomposing the mesh into regular slices cut along the z-coordinate axis.

4 Validation of the Numerical Technique

In order to validate the implementation of vibrational relaxation, we perform two tests for acoustic wave propagation only, one with a background flow and the other without. We do not present validation for gravity waves since the impact of vibrational relaxation on their propagation is very weak (relaxation frequencies of CO_2 on Mars are much larger than the expected dominant frequencies of gravity waves) and gravity waves without such relaxation process were already validated in Brissaud et al. (2016).

The source is set as a pressure fluctuation and is implemented in (1)-1 as

$$\partial_t p = -\mathbf{w}.\nabla p - \rho c^2(\nabla.\mathbf{v} + S) - \rho \mathbf{v}.\mathbf{g} + e_1, \tag{20}$$

Table 1 Simulation parameters corresponding to the homogeneous isothermal model for the validation case in Sect. 4. The parameters have the following dimensions: ρ (kg·m^{-3}), c (m·s^{-1}), η_V (kg·m^{-1}·s^{-1}), μ (kg·m^{-1}·s^{-1}), τ_ϵ, τ_σ (s), g_z (m·s^{-2}) and w_x (m·s^{-1})

$L_x \times L_z$ (km)	Δx (m)	$\Delta t(s)$	ρ	c	(η_V, μ)	$(\tau_\epsilon, \tau_\sigma)$	g_z	w_x
200×100	100	10^{-2}	1.77×10^{-2}	236	$(0, 0)$	$(1.5, 1)$	0	0

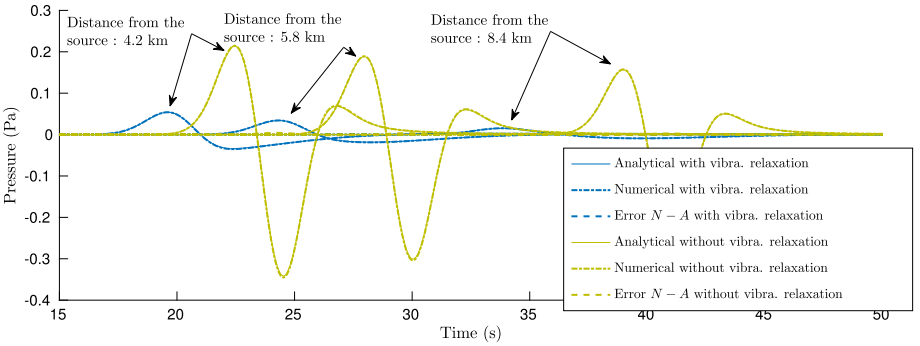

Fig. 2 Pressure from the numerical solution with vibrational relaxation set to $\tau_\epsilon = 1.5$ s and $\tau_\sigma = 1$ s ('Numerical with vibra. relaxation') and the analytical solution with vibrational relaxation ('Analytical with vibra. relaxation') as well as the difference between the two ('Error N-A with vibra. relaxation'). The numerical solution without vibrational relaxation ('Numerical without vibra. relaxation'), the analytical solution without vibrational relaxation ('Analytical without vibrat. relaxation') as well as the difference between the two ('Error N-A without vibra. relaxation') are also presented. The signals are shown through time for the simulation in Sect. 4.1, i.e. the windless validation case, at three recording stations located at the same altitude $z = 10$ km, their position along x being $x = 4.2$, 5.8 and 8.4 km from left to right. The atmosphere is considered isothermal (Table 1)

where the source S is time-dependent variable and reads

$$S(\mathbf{x}, t) = -2(t - t_0)e^{-\{\pi f_0 (t-t_0)\}^2} \delta(\mathbf{x_s}), \tag{21}$$

where δ is the Kronecker symbol, $\mathbf{x_s}$ the source position, $t_0 = 5$ s the source onset time and $f_0 = 5$ Hz the source dominant frequency. Using the formulation of the pressure response in Appendix 1 for a viscous medium subject to wind, one can compute an analytical solution for this simulation case.

4.1 Vibrational Relaxation Windless Validation Case

Table 1 summarizes the physical and numerical parameters used for the simulation. The choice of relaxation times $(\tau_\epsilon, \tau_\sigma)$ corresponds to a relaxation frequency $f_r = \frac{1}{2\pi\sqrt{\tau_\epsilon \tau_\sigma}} = 0.13$ Hz close to the dominant frequency of the source, in order to clearly see the effect of the vibrational relaxation.

In Fig. 2, results show a very good fit in terms of amplitude, with a maximum error that is less than 4 %. Vibrational relaxation clearly impacts the amplitude but also the velocity of the wave.

In Fig. 3 one notices that as the frequency increases the group velocity of the wave packet increases as well and becomes larger than the adiabatic sound velocity. This means that

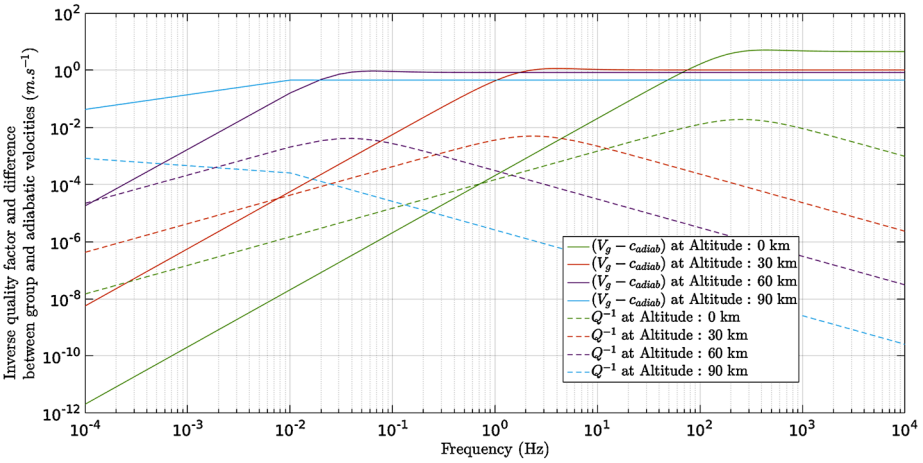

Fig. 3 Difference between the group and adiabatic velocity and inverse quality factor versus frequency in the range $[10^{-4}, 10^{4}]$ Hz in an atmosphere subject to vibrational relaxation at various altitudes $z = 0, 30, 60, 90$ km. The atmosphere model is based on the Mars Climate Database. One notices that as frequency increases the group velocity of the wave packet increases as well and becomes larger than the adiabatic sound velocity

Table 2 Simulation parameters corresponding to the homogeneous isothermal model for the validation case in Sect. 4.2. The parameters have the following dimensions: ρ (kg·m^{-3}), c (m·s^{-1}), η_V (kg·m^{-1}·s^{-1}), μ (kg·m^{-1}·s^{-1}), τ_ϵ, τ_σ (s), g_z (m·s^{-2}) and w_x (m·s^{-1})

$L_x \times L_z$ (km)	Δx (m)	Δt (s)	ρ	c	(η_V, μ)	$(\tau_\epsilon, \tau_\sigma)$	g_z	w_x
200×100	100	10^{-2}	1.77×10^{-2}	236	$(0, 0)$	$(1.5, 1)$	0	40

waves undergoing vibrational effects will propagate faster than waves in a non-attenuating model. This figure also shows the inverse quality factor as a function of frequency due to vibrational relaxation. It validates the high-Q assumption ($Q \gg 1 \Leftrightarrow Q^{-1} \ll 1$) for our frequency range since at any altitude $Q^{-1} < 0.05$.

4.2 Vibrational Relaxation Windy Validation Case

Table 2 summarizes the physical and numerical parameters used for the simulation.

In Fig. 4, results show a very good fit in terms of maximum amplitude error which is less than 4 %. As in the simulation in Sect. 4.1, vibrational relaxation impacts the propagation by damping the wave amplitude and by increasing phase and group velocities. But, in this case the wind also plays a significant role by shifting the wave apparent frequency and then by modifying its phase and amplitude. One interesting feature is that upwind waves, which should have larger amplitudes than downwind ones (see signal 'Upwind without vibrational relaxation' in Fig. 5 which is a typical feature of the Doppler shift), have lower amplitude here due to vibrational relaxation. Indeed, as the wind shifts the upwind wave dominant frequency into the vibrational relaxation frequency range where its impact is significant, the upwind wave will undergo more damping from vibrations of CO_2 than the downwind one.

Figure 5 shows simulation results at the same locations with and without vibrational relaxation. One notices that waves in the medium without vibrational relaxation have a larger

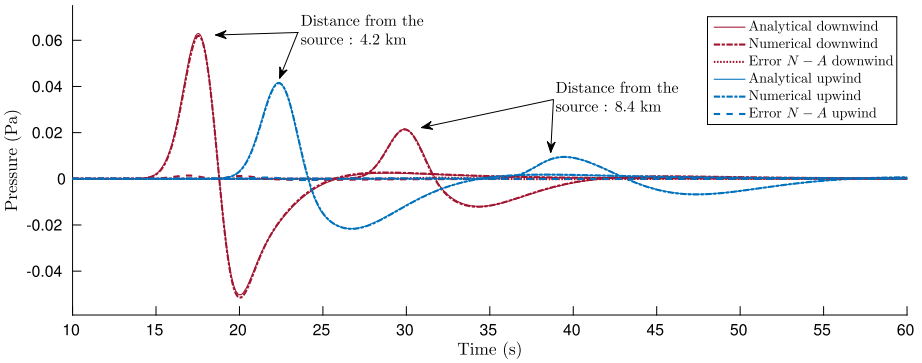

Fig. 4 Pressure from the numerical solution at downwind recording stations ('Numerical downwind'), at upwind stations ('Numerical upwind') and the corresponding analytical signals ('Analytical downwind' and 'Analytical upwind') as well as the difference between them ('Error N-A downwind' and 'Error N-A upwind'). The signals are shown through time for the simulation in Sect. 4.2, i.e. the windy validation case, at two recording stations located at the same altitude $z = 10$ km, their position along x being $x = 4.2$ and 8.4 km from left to right. The atmosphere is considered isothermal with vibrational relaxation $\tau_\epsilon = 1.5$ s and $\tau_\sigma = 1$ s (Table 2)

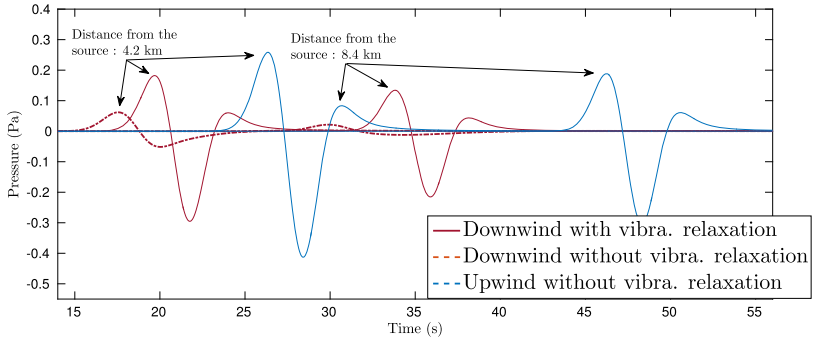

Fig. 5 Pressure from the numerical solution at downwind recording stations with vibrational relaxation set to $\tau_\epsilon = 1.5$ s and $\tau_\sigma = 1$ s ('Downwind with vibra. relaxation') and the solution at upwind and downwind stations without vibrational relaxation ('Upwind without vibra. relaxation' and 'Downwind without vibra. relaxation'). The signals are shown through time for the simulation in Sect. 4.2, i.e the windy validation case, at two recording stations located at the same altitude $z = 10$ km, their position along x being $x = 4.2$ and 8.4 km from left to right. The atmosphere is considered isothermal (Table 2)

amplitude than in the medium with vibrational relaxation, as expected, where the amplitude becomes strongly damped and the wave apparent frequency shifted as the wave travels through the medium.

5 Applications to Mars Atmospheric Signals

In this section, we explore applications of our simulation tool to the pressure signals generated by a meteor impact on Mars ground.

5.1 Pressure Signal from a Meteor Impact

Acoustic and gravity waves emitted by a meteor are either due to the shock wave along the track during re-entry, to atmospheric explosions corresponding to fragmentation of the meteor during re-entry, or to meteor and target vaporisation at the impact (Edwards 2010). Even if our simulation tool allows to insert pressure sources anywhere in the domain, we will only consider pressure waves created by meteor impacts on the ground. The reason for this choice is that most of the meteors that will generate direct seismic waves detectable by INSIGHT seismometer will impact the ground (Popova et al. 2003; Chappelow and Sharpton 2006). The characteristics of the atmospheric pressure signals emitted during a hyper-velocity impact on the ground are poorly documented because such signals are rarely observed on Earth, for which pressure signals emitted during meteor events is coming from airbursts (explosions in the atmosphere) (Edwards 2010). To our knowledge, only two observations of pressure waves associated with the impact of a meteor on the ground are documented, for the 1908 Tunguska event in Siberia (Whipple 1930) and for the 2007 Carancas event in Bolivia (Pichon et al. 2008; Tancredi et al. 2009). The interpretation of these measurements are still debated, with a poorly known proportion of the signal coming either from a low altitude airburst or from the surface impact. However, the radiation pattern of an hyper-velocity impact source in the solid is close to the one of an explosion (Walker 2003). Consequently, the atmospheric acoustic source is simulated here through an explosion. The scaling of over-pressure and dominant period of the signal with the characteristics of the impactor is also difficult to evaluate because these parameters strongly depend respectively on the impactor trajectory and impactor diameter (Haynes and Millet 2013).

Thus, we postpone the quantification of source parameters to future studies. The source used in our simulations is the one described by (21), which corresponds to a volume decrease, at constant mass, due to the additional air mass provided by the vaporisation of the impactor and of part of the target, followed by a volume increase. No additional scaling is provided for its amplitude, and a dominant frequency of 0.1 Hz is chosen to fit values expected in the far field (Haynes and Millet 2013). Our simulations are linear, so the amplitude of simulated records can be multiplied by the expected over-pressure at the source to obtain true amplitudes.

5.2 Mars Atmosphere Models

Typical vertical profiles of thermodynamical properties, composition and winds in the Martian atmosphere are extracted from the Mars Climate database (MCD) (Lewis et al. 1999) which compiles the outputs from simulations performed with the Laboratoire de Météorologie Dynamique (LMD) Global Climate Model (GCM) (Forget et al. 1999). The latest version (v5.2) of the MCD is employed here to benefit from the latest improvements. The treatment of near-surface (Colaïtis et al. 2013) and thermosphere (González-Galindo et al. 2009) processes are of peculiar interest in this study. The location at which the atmospheric profiles are extracted from the MCD is chosen to be equatorial, at the approximate INSIGHT lander location (135.7° E, 4.4° N). From pressure, density, temperature and composition values, we compute the sound speed, Brunt-Väisälä frequency, and attenuation parameters (Bass and Chambers 2001).

A first model going from the surface to 200 km altitude is presented in Fig. 6 at midday and midnight for solar longitudes of 90° and 240°. Those values of solar longitude correspond to, respectively, northern summer solstice and late southern spring seasons (martian solar longitude is 0° for northern spring equinox), and were chosen as both typical from

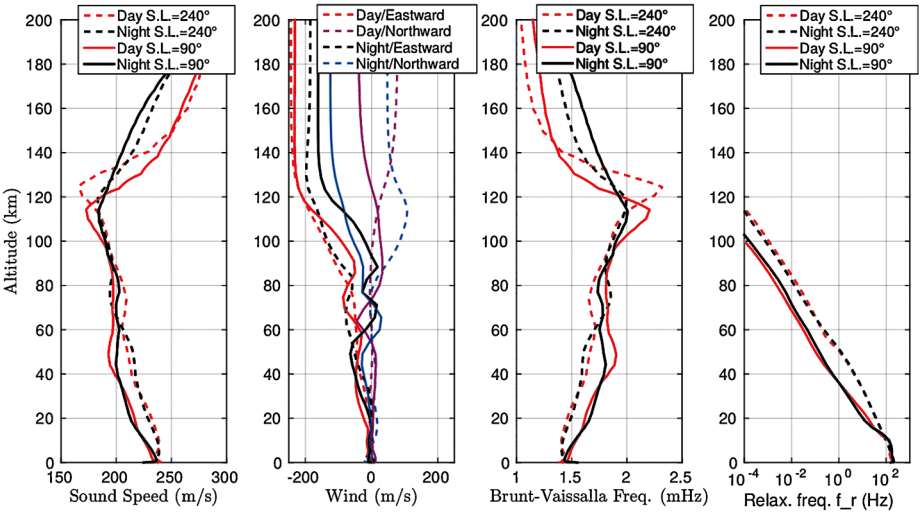

Fig. 6 From left to right, sound speed (in $m{\cdot}s^{-1}$), Eastward and Northward winds (in $m{\cdot}s^{-1}$) corresponding to positive values of respectively zonal and meridional wind components, Brunt-Väisälä frequency (in mHz) and peak relaxation frequency of CO_2 vibrational modes (in Hz) as a function of altitude (in km). Results are presented for 12 h (*red* or *magenta*) and 0 h (*black* or *cyan*) Local Times (LT), and for 240° (*dashed lines*) and 90° (*solid lines*) of solar longitude. These parameters are computed from values extracted from Mars Climate Data base version 5.2 (MCD5.2) and (Bass and Chambers 2001)

a climatic standpoint (i.e. diurnal and seasonal variability) and extreme from an acoustic standpoint (different altitudes for sound speed and wind extrema). Figure 6 illustrates how diurnal and seasonal variability impact the parameters relevant to acoustic-gravity waves. The sound speed decreases from the surface to about 120 km altitude. The wind components are positive in the Eastward and Northward directions. The horizontal wind vector is strong and variable above 20 km, but still significant for acoustic propagation in the first 10 km. The profile of Brunt-Väisälä frequency continuously increases up to 120 km altitude, which favors gravity wave trapping close to this altitude. The overall shapes of sound speed and Brunt-Väisälä frequency profiles imply that, in the absence of wind, acoustic and gravity waves emitted on ground are not ducted back to the surface until they reach about 120 km altitude. The peak frequency of CO_2 vibrational relaxation affects the infrasonic frequency range in the altitude range starting from 35–50 km up to 80–90 km, depending on the season.

5.3 Wave Refraction by High-Altitude Wind Ducts

Ray trajectories and travel times (Dessa et al. 2005), and simulated waveforms of acoustic signals generated by a meteor impact on the ground are presented in Figs. 7, 8 and 9. These simulations are performed for the day-side model (12 h Local Time) at 90° of solar longitude along a West-East plane (solid red curves in Fig. 6). Grid cells of 250 m × 250 m, over a 1000 km × 200 km domain with a time step of 2×10^{-3} s are used for a source of 10 s dominant period. The effective sound speed (sound velocity corrected for the horizontal wind effect) increases upward for a downwind propagation. Therefore, the records in this direction (blue curves, West direction) present, in addition to direct wave arrivals, late arrivals that correspond to wave refractions at local maxima of wind at 30, 70 and 130 km

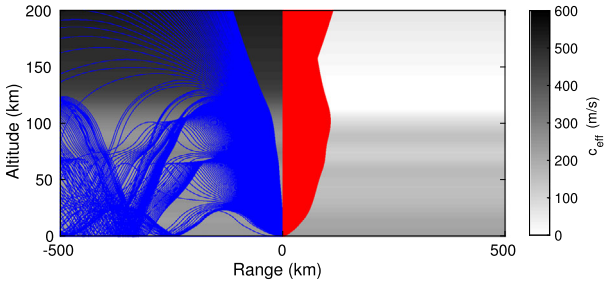

Fig. 7 Ray trajectories in the West (*left*) to East (*right*) plane at 90° solar longitude and 12 h local time. The *background color scale* indicates effective sound velocity with *black* and *white colors* indicating highest and lowest effective velocities respectively

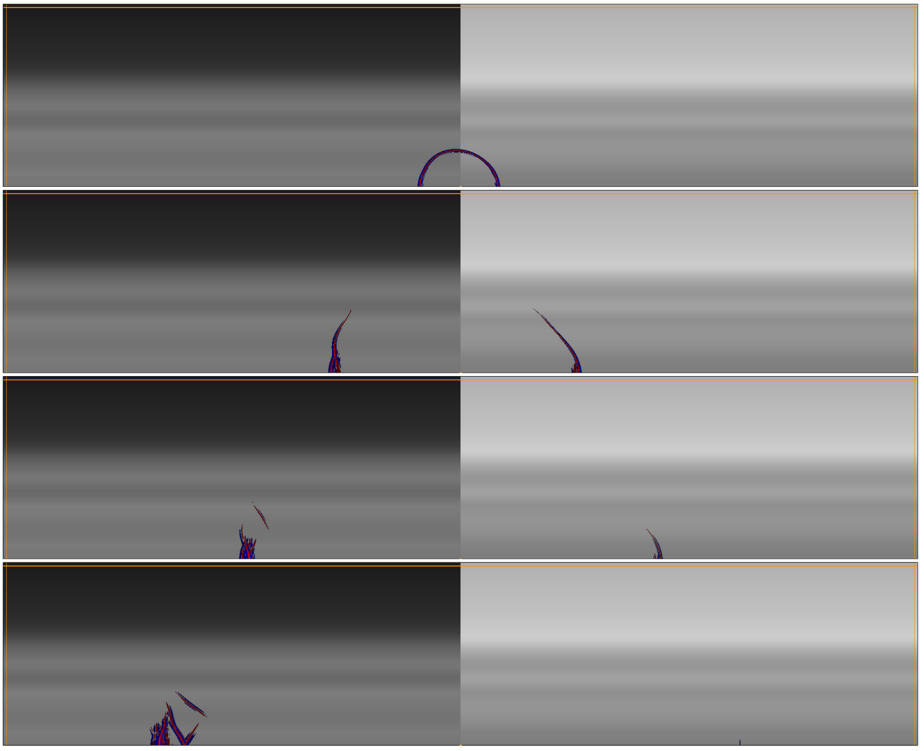

Fig. 8 Snapshots of simulated pressure perturbations (in Pa, scaled independently to maximum value over the whole domain) at times 200 s, 600 s, 1000 s and 1400 s from top to bottom. *Blue* and *red colors* indicate negative and positive pressure perturbations respectively. The *background color scale* indicates effective sound velocity (sound speed plus wind) in the two different propagation directions (West and downwind on the *left*, East and upwind on the *right*) with *black* and *white colors* indicating highest and lowest effective velocities respectively. Simulation domain is 1000 km wide and 200 km high, and the surface impact source is located in the *middle*. The *orange lines* indicate the entrance of the PML regions

altitudes whereas none of the simulated rays are ducted back to the surface in the case of an upwind propagation (red curves, East propagation). In Fig. 9, the ray arrival times of waves refracted back to the surface are also indicated for both Cartesian and spherical geometries. The Cartesian arrival times correctly fit the wave packet arrivals, even if ray theory does not reproduce all the waveform complexities. The delays between Cartesian and spherical geometry increase with arrival time, reaching up to 30 seconds.

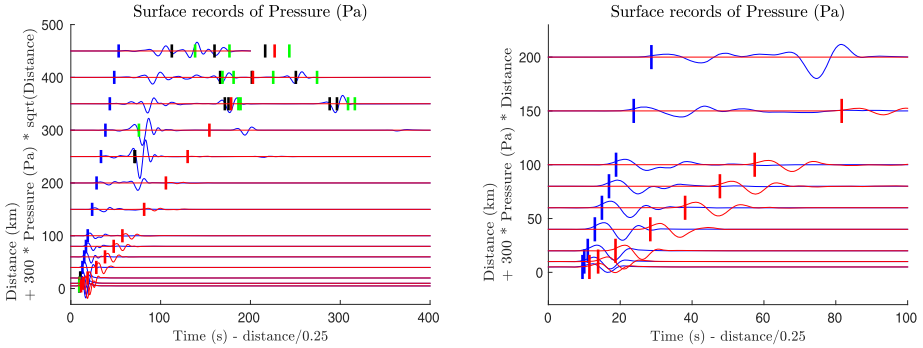

Fig. 9 Simulated surface records sorted by distance (in km) as a function of reduced time (in s) for all the simulated surface records (*left*) and for a zoom on the closest distances to the source (*right*). Reduced time induces a shift of the records in the left direction by Distance/0.25 seconds to ensure a better readability of the figure. The amplitude of the records is scaled according to the formula provided in the y-axis label for the same reason. Downwind/West (resp. upwind/East) records are indicated in *blue* (resp. in *red*). Rays theoretical arrival times for direct waves are indicated by *thick blue* and *red tags*. For waves refracted on the 30 km, 70 km and 130 km wind ducts, ray arrival times are indicated both for computations in Cartesian (*black tags*) and in spherical (*green tags*) geometry

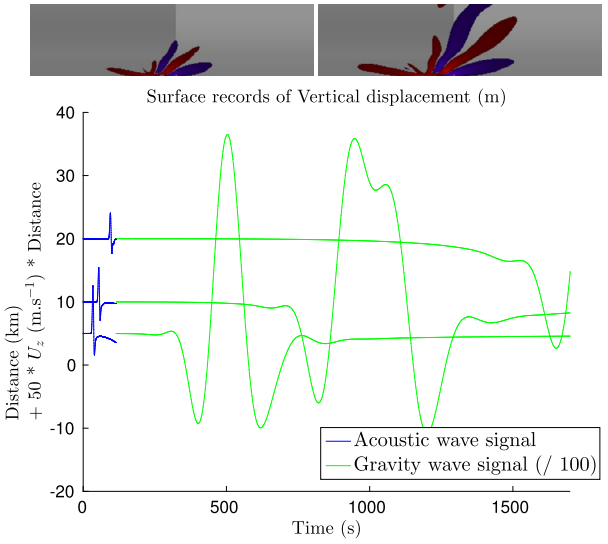

Fig. 10 On the top, two snapshots of vertical displacement (in m) at $t = 1600$ s (*left*) and $t = 1800$ s (*right*) focused on a domain of size 184×23.25 km around the source. The *red* and *blue colors* indicate positive and negative vertical displacements respectively. The *background color scale* indicates effective sound velocity with *black* and *white colors* indicating highest and lowest effective velocities respectively. On the bottom, zoom on simulated vertical displacement records close to the impact source as a function of distance (in km) and time (in s). The first 115 seconds of the records are presented in *blue* with a scale given in the label of the *vertical axis*. The latter part of the same records are presented in *green* with a scaling 100 times smaller

Meteor impacts generate also gravity waves which are observed in our simulations. Figure 10 presents snapshots of gravity wave propagation near the source. One notices that the energy propagates towards the top left and top right of the domain whereas the phase prop-

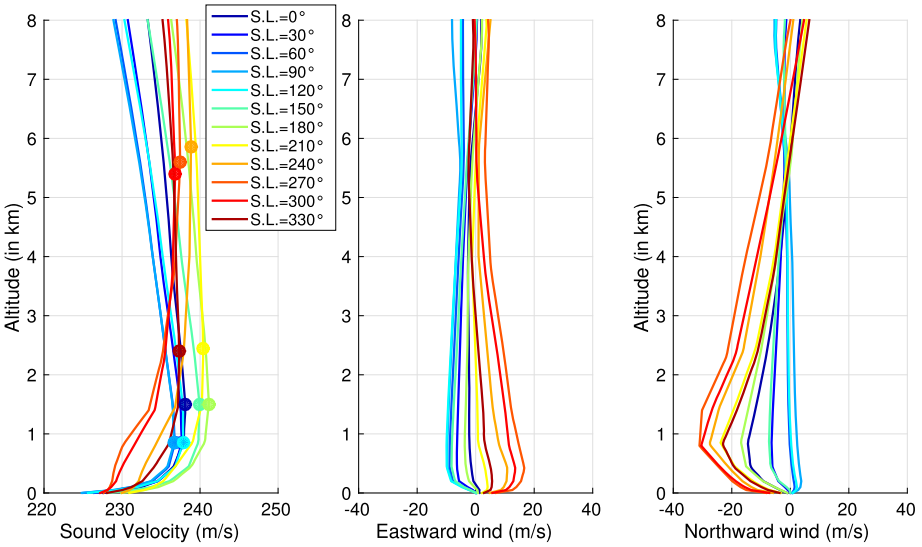

Fig. 11 From left to right, sound speed (in $m{\cdot}s^{-1}$), Eastward and Northward winds (in $m{\cdot}s^{-1}$) as a function of altitude (in km) for different values of solar longitude (the different colors) for nightside conditions (0 h local time). *Filled circles* indicate the altitude of maximum sound speed

agates orthogonally to it, a typical feature of gravity waves. The wave pattern is strongly influenced by winds, with downwind waves ducted back to the surface, and upwind waves propagation upward (Ding et al. 2003). Another effect of background wind is the displacement of the whole gravity wave train in the downwind direction. As a consequence, the downwind records at the surface present both acoustic and gravity wave trains. The gravity wave signals arrive much later than acoustic waves, and present lower frequencies. Due to the dominant period of the source, chosen in the acoustic range, the gravity wave amplitude is low on pressure records. That is why surface records are plotted here for vertical displacement for which direct and horizontally propagating acoustic waves have a low amplitude. However, for the true meteor impact source, we expect the excited frequency range to be larger than in our simulation, thus generating gravity waves with larger amplitudes than the ones presented here. If the impact space/time location is known, the arrival times of both wave types can be used to infer wind profiles along the path. The sensitivity of differential arrival times between acoustic and gravity waves to source location and wind profiles will be inferred in future studies.

5.4 Acoustic Wave Trapping Close to the Surface at Night

In this section, we present simulation results for acoustic wave propagation in the first 10 km of the atmosphere on the night-side. Figure 11 presents the evolution of sound speed and winds as a function of the season (solar longitude) at midnight. Due to the radiative cooling of the surface at night, the atmosphere presents a strong thermal gradient in its first kilometers. Consequently, sound speed increases from the cold surface to a maximum value comprised between 0.8 and 6 km altitude depending on the season. This feature creates a waveguide close to the surface (at minimum sound speed). Acoustic wave propagation is also sensitive to wind profiles. As shown in Fig. 11 the wind significantly varies with the

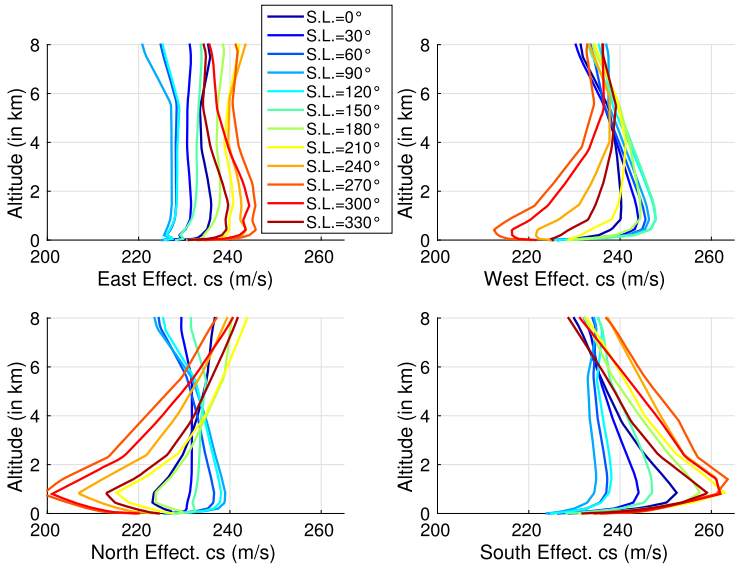

Fig. 12 Effective sound speed (in $m{\cdot}s^{-1}$) for nightside conditions (0 h local time) as a function of altitude (in km) and solar longitude (the different colors) for different wave propagation directions: East (*top left*), West (*top right*), North (*bottom left*) and South (*bottom right*)

season, both in direction and amplitude. However, the wind amplitude decreases to values lower than 8 $m{\cdot}s^{-1}$ around 6 km altitude in all cases. Fig. 12 presents the effective sound speed profiles (sound speed plus wind) as a function of altitude and season for different wave propagation directions. The various wind patterns induce very different situations depending on the season and propagation directions. However, some common patterns can be described. Solar longitudes close to 90° (blueish colors, low winds) generate sound waveguides in the first kilometer of Mars atmosphere. Solar longitudes close to 240° (reddish colors, high winds) generate waveguides of 5–6 km thickness, except for downwind propagation in the southern direction, for which the waveguide in the first kilometer is mainly controlled by the strong vertical wind gradient.

In order to illustrate acoustic wave trapping close to the surface at night, Figs. 13 and 14 present simulations for night-side conditions (0 h Local Time) at a solar longitude of 240° in the North-South plane close to the surface. These simulations are performed with grid cells of 50 m × 50 m, over a 200 km × 40 km domain with a time step of 10^{-3} s for a source of 10 s dominant period. For wave propagation in the southern direction (blue color), the kilometer scale waveguide traps rays, as observed at the bottom of Fig. 13, but the numerical simulation does not reproduce this wave trapping because the dominant wavelength (about 2.5 km) is larger than the waveguide thickness. If the effect of the kilometer scale waveguide is neglected, the waves emitted at the surface in the southern direction propagate upward and do not come back to the surface. On the contrary, the waves emitted in the northern direction are trapped in a waveguide in the first 10 km of the atmosphere. In Fig. 14(a) the first wave reflected back to the surface at the top of the waveguide clearly appears for distances larger than 30 km. As shown in Fig. 14(b), due to the wave trapping and to upwind propagation of direct waves, the amplitude of pressure signals in the northern direction remains almost constant in the 20 to 90 km distance-range. The surface waveguides will efficiently trap waves depending on their frequency content. The single dominant frequency simulated here

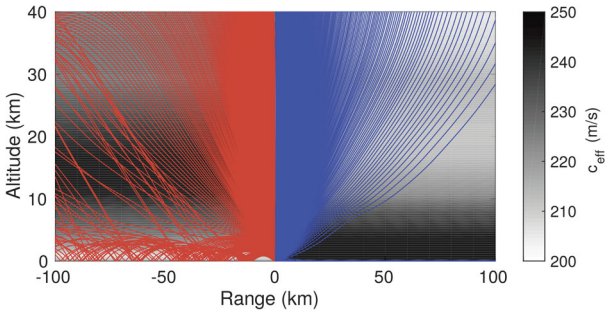

Fig. 13 Ray trajectories in the North (*left*) to South (*right*) plane at 240° solar longitude and 0 h local time. The *background color scale* indicates effective sound velocity with *black* and *white color* indicating highest and lowest effective velocities respectively

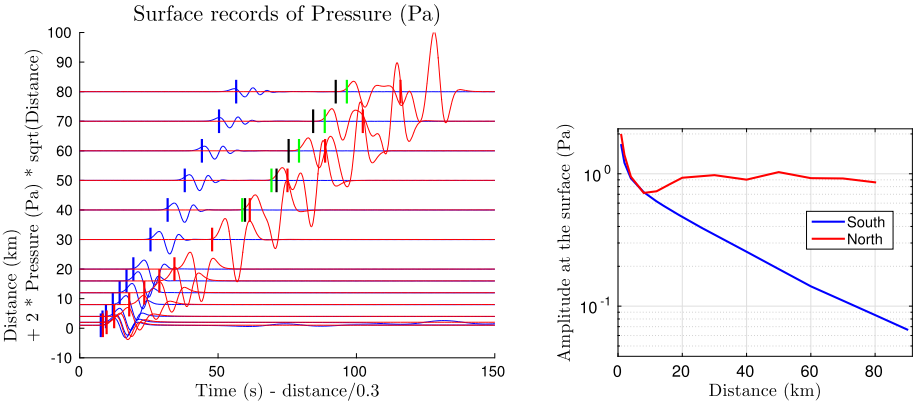

Fig. 14 On the *left*, simulated surface records sorted by distance (in km) as a function of reduced time (in s). Reduced time induces a shift of the records in the left direction by Distance/0.3 seconds to ensure a better readability of the figure. The amplitude of the records is scaled according to the formula provided in y-axis label for the same reason. Rays theoretical arrival times for direct waves are indicated by thick blue and red tags. The arrival times of rays reflected back to the surface at the top of the waveguide are indicated both for computations in Cartesian (*black tags*) and in spherical (*green tags*) geometry. On the *right*, maximum amplitude (in Pa) measured on simulated records as a function of distance to the source (in km). North (resp. South) stations are indicated in *red* (resp. in *blue*)

is sensitive to waveguide thicknesses larger than about 3 km. But more realistic broad band impact sources will generate high frequency waves that will be trapped in kilometer scale waveguides.

5.5 Future Application to the INSIGHT Mission

The INSIGHT NASA discovery mission will deploy seismic, pressure, wind and magnetic sensors in the Elysium planitia region (Banerdt et al. 2013). The low topography of this region is favorable to detect acoustic waves trapped in the night-side waveguide. The pressure sensor is designed to correct the seismometer for pressure effects. Therefore, it has a high sampling rate (20 Hz), a low noise in the seismic/infrasonic frequency range, a wind filtering inlet and continuous recordings synchronized with seismic recordings (Banfield and InSight Science Team 2014). In addition, a wind sensor will provide wind amplitude and direction 1 m above the surface. Consequently, the INSIGHT instruments are suited to detect acoustic waves from meteor impacts. Our study demonstrates that this may be possible at night. In

addition, the wind sensor will allow vertical wind profiles provided by climate models to be calibrated, thus improving the reliability of atmosphere models at impact times. Finally, the thermal noise on the pressure sensor, which is the dominant noise source at low frequencies, will be minimized by its design, thus long period gravity waves created by impacts may also be detected by the sensor.

6 Conclusions and Future Work

We have presented a finite-difference full wave simulation tool for acoustic and gravity wave propagation in Mars atmosphere, and have validated it by comparing with analytical solutions and with acoustic ray tracing. This code properly takes into account the effects of exponential density decay, sound velocity variations, wave attenuation and horizontal winds. The application of this numerical technique to realistic Mars atmosphere models has allowed us to study the potential interest of a surface infrasonic sensor for the detection of meteor impacts on the surface. Our simulations demonstrate that such a detection for day-side conditions is only possible for waves propagating downwind, for which a part of the acoustic wavefront is refracted back to the surface by wind ducts. However, at night, a waveguide is present close to the surface that would allow for long distance propagation of acoustic signals in flat areas. Such theoretical results should soon be applicable to pressure measurements from the INSIGHT NASA Discovery mission.

In the near future, this study will be completed by a sensitivity study of acoustic and gravity waves to source location and wind profiles. In addition, for a more direct application to INSIGHT measurements, the pressure wave amplitude as a function of meteor impact parameters will be estimated and compared to the expected background noise.

Acknowledgements We acknowledge Don Banfield and an anonymous reviewer for their detailed review of the manuscript. We thank the INSIGHT science team for fruitful discussions. We also thank the "Région Midi-Pyréenées" (France) and "Université fédérale de Toulouse" for funding the PhD grant of Quentin Brissaud. This study was also supported by CNES through space research scientific projects. Computer resources were provided by granted projects No. p1138 at CALMIP computing centre (Toulouse France), Nos. t2014046351 and t2015046351 at CEA centre (Bruyères, France). This is Insight Contribution Number 16.

Appendix 1: Analytical Solution for Acoustic Wave Propagation in a Windy Homogeneous Atmosphere with Vibrational Relaxation

In the framework of acoustic wave propagation in a windy homogeneous medium with vibrational relaxation, the state and momentum equations read

$$\begin{aligned}(\partial_t + \mathbf{w}.\nabla)p &= -\nabla.\mathbf{v} * \Phi - \rho c^2 S,\\ \rho(\partial_t + \mathbf{w}.\nabla)\mathbf{v} &= -\nabla p,\end{aligned} \tag{22}$$

where, $\forall t \in \mathbb{R}^+$

$$\Phi(t) = H(t) * \psi(t), \tag{23}$$

with H the Heaviside function and ψ the relaxation function of the viscoelastic medium considered.

Taking the divergence of (22)-2 yields

$$(\partial_t + \mathbf{w}.\nabla)\nabla.\mathbf{v} = -\frac{1}{\rho}\Delta p, \tag{24}$$

where Δ is the Laplacian operator. Thus, taking the total derivative D_t (where $D_t = \partial_t + \mathbf{v}\nabla$) of (22)-1 yields

$$\begin{aligned}(\partial_t + \mathbf{w}.\nabla)^2 p &= -\nabla.(\partial_t + \mathbf{w}.\nabla)\mathbf{v} * \Phi - (\partial_t + \mathbf{w}.\nabla)S \\ &= \frac{1}{\rho}\Delta p * \Phi - \rho c^2(\partial_t + \mathbf{w}.\nabla)S.\end{aligned} \tag{25}$$

By considering, in (25), plane wave solutions of the form $p = \tilde{p}e^{-i\omega t}$ and Ψ, defined in (16), the relaxation function for a Zener mechanism (Carcione et al. 1988), we can perform the complex integration of the convolution term

$$\begin{aligned}\Delta\tilde{p}\int_{-\infty}^{\infty} e^{-i\omega t}\tilde{\Phi}H dt &= \Delta\tilde{p}\int_{-\infty}^{\infty} e^{-i\omega t}\frac{1}{\tau_\epsilon}\left(1 - \frac{\tau_\epsilon}{\tau_\sigma}\right)e^{-\frac{t}{\tau_\sigma}}H dt \\ &= \Delta\tilde{p}\frac{1}{\tau_\epsilon}\left(1 - \frac{\tau_\epsilon}{\tau_\sigma}\right)\int_0^{\infty} e^{-(i\omega + \frac{1}{\tau_\sigma})t}dt \\ &= \Delta\tilde{p}\frac{1}{\tau_\epsilon}\left(1 - \frac{\tau_\epsilon}{\tau_\sigma}\right)\frac{1 + i\omega\tau_\epsilon}{1 + i\omega\tau_\sigma}\end{aligned} \tag{26}$$

then, from the plane wave form in the Fourier space ($\partial_t = -i\omega$), and one can recast (25) as

$$(-i\omega + \mathbf{w}.\nabla)^2\tilde{p} = \frac{\hat{K}_c}{\rho}\Delta\tilde{p} - \rho c^2(-i\omega + \mathbf{w}.\nabla)\tilde{S}. \tag{27}$$

The tilde denotes the time Fourier transform and $\hat{K}_c$ is the complex bulk modulus, in the case of a single relaxation mechanism, which reads (Carcione et al. 1988)

$$\hat{K}_c = \rho c^2\frac{1 + i\omega\tau_\epsilon}{1 + i\omega\tau_\sigma} = \rho\hat{c}^2, \tag{28}$$

where the complex velocity $\hat{c}$ reads

$$\hat{c} = c\sqrt{\frac{1 + i\omega\tau_\epsilon}{1 + i\omega\tau_\sigma}} \tag{29}$$

The complex equation (27) can then be expanded as

$$\begin{gathered}
\left(-\omega^2 + w_x^2\partial_x^2 - 2i\omega w_x\partial_x\right)\tilde{p} = \frac{\hat{K}_c}{\rho}\left(\partial_x^2 + \partial_z^2\right)\tilde{p} - \rho c^2(-i\omega + \mathbf{w}.\nabla)\tilde{S}, \\
\left\{\frac{\rho}{\hat{K}_c}\left(-\omega^2 + w_x^2\partial_x^2 - 2i\omega w_x\partial_x\right) - \partial_x^2 - \partial_z^2\right\}\tilde{p} = -\frac{\rho^2}{\hat{K}_c}c^2(-i\omega + \mathbf{w}.\nabla)\tilde{S}, \\
\left\{\frac{\rho}{\hat{K}_c}\left(\omega^2 - w_x^2\partial_x^2 + 2i\omega w_x\partial_x\right) + \partial_x^2 + \partial_z^2\right\}\tilde{p} = \frac{\rho^2}{\hat{K}_c}c^2(-i\omega + \mathbf{w}.\nabla)\tilde{S}, \\
\left\{\frac{1}{\hat{c}^2}\left(\omega^2 - w_x^2\partial_x^2 + 2i\omega w_x\partial_x\right) + \partial_x^2 + \partial_z^2\right\}\tilde{p} = \frac{\rho c^2}{\hat{c}^2}(-i\omega + \mathbf{w}.\nabla)\tilde{S}, \\
\left(\partial_x^2 + \partial_z^2 + \hat{k}^2 + 2i\hat{k}\hat{M}\partial_x - \hat{M}^2\partial_x^2\right)\tilde{p} = -\frac{\rho c^2}{\hat{c}^2}(-i\omega + \mathbf{w}.\nabla)\tilde{S},
\end{gathered} \tag{30}$$

with $\hat{M}$ the Mach number, that is,

$$\hat{M} = \frac{w_x}{\hat{c}} = \frac{w_x}{c\frac{1+i\omega\tau_\epsilon}{1+i\omega\tau_\sigma}}, \tag{31}$$

where $\hat{c}$ is the complex velocity and k is the wavenumber $\hat{k} = \frac{\omega}{\hat{c}}$. The hat over $\hat{M}$ and $\hat{k}$ is introduced to differentiate from the usual Mach and wave numbers in an inviscid medium.

Finally, we will consider

$$\tilde{S} = \frac{2i\,\tilde{A}\hat{K}_c}{\omega\rho c^2}e^{-i\omega t}\delta_x\delta_z, \tag{32}$$

where δ_x, δ_z are the Kronecker delta symbols, and $\tilde{A}$ is the Fourier transform of the amplitude of the time-dependent source function, that is,

$$A(t) = -2(\pi f_0)^2(t - t_0)e^{-\{\pi f_0(t-t_0)\}^2}. \tag{33}$$

We use the same method as in Ostashev et al. (2005) to obtain the pressure response in this framework, that is

$$\tilde{p} = \frac{i\,A}{2(1-\tilde{M})^{3/2}}\left(H_0^1(\xi) - \frac{i\,\tilde{M}\cos\beta}{\sqrt{1-\tilde{M}^2\sin\beta^2}}H_1^1(\xi)\right)e^{\frac{-i\tilde{k}\tilde{M}R\cos\beta}{1-\tilde{M}^2}}, \tag{34}$$

where $(H_i^1)_{i=1,2}$ are the Hankel functions of first kind, and ξ reads

$$\xi = \frac{\tilde{k}R\sqrt{1-\tilde{M}^2\sin\beta^2}}{1-\tilde{M}^2}. \tag{35}$$

Using Hankel function asymptotic (Abramowitz and Stegun 1964) by considering the approximation $|\tilde{k}R| >> 1$, yields

$$\tilde{p} = \frac{A(\sqrt{1-\tilde{M}^2\sin\beta^2} - \tilde{M}\cos\beta)}{\sqrt{2\pi\tilde{k}R}(1-\tilde{M}^2)(1-\tilde{M}^2\sin\beta^2)^{3/4}}e^{\frac{i}{1-\tilde{M}^2}(\sqrt{1-\tilde{M}^2\sin\beta^2} - \tilde{M}\cos\beta)\tilde{k}R + \frac{i\pi}{4}}. \tag{36}$$

Appendix 2: Numerical Implementation of ADE-PML for a Medium Subject to Gravity

This boundary condition corresponds to mesh stretching in the boundary layer which requires to recast the derivatives in the new stretched set of complex-valued coordinates (Komatitsch and Martin 2007). We do this using ADE-PML memory variables. In this new reference frame (19) read

$$\begin{aligned}
\partial_t p &= -\mathbf{w}.\tilde{\nabla} p - \rho c^2 \tilde{\nabla}.\mathbf{v} - \tilde{\nabla} p_0 \mathbf{v} + e_1,\\
\partial_t \rho_p &= -\mathbf{w}.\tilde{\nabla}\rho_p - \tilde{\nabla}.(\rho\mathbf{v}),\\
\rho\partial_t \mathbf{v} &= -\rho\big\{(\mathbf{v}.\tilde{\nabla})\mathbf{w} + (\mathbf{w}.\tilde{\nabla})\mathbf{v}\big\} + \tilde{\nabla}.\boldsymbol{\Sigma} + \tilde{\mathbf{g}}\rho_p,\\
\partial_t e_1 &= -\frac{1}{\tau_\sigma}\left[\left(1 - \frac{\tau_\sigma}{\tau_\epsilon}\right) + e_1\right],
\end{aligned} \tag{37}$$

with

$$(\boldsymbol{\Sigma})_{ij} = -p\delta_{ij} + \mu\left(\tilde{\partial}_j(\mathbf{v}+\mathbf{w})_i + \tilde{\partial}_i(\mathbf{v}+\mathbf{w})_j - \frac{2}{3}\delta_{ij}\tilde{\nabla}.\mathbf{v}\right) + \eta_V \delta_{ij}\tilde{\nabla}.\mathbf{v}.$$

Note that we wrote the pressure equation (37)-1 in terms of the ambient pressure p_0 rather than in terms of its value coming from hydrostatic equilibrium (i.e. in the interior domain $\nabla p_0 = \rho\mathbf{g}$). Indeed, as we stretch coordinates the hydrostatic equilibrium equation is also modified as

$$\tilde{\nabla} p_0 = \rho\mathbf{g}. \tag{38}$$

In this new reference frame derivatives will read, for any unknown ϕ

$$\tilde{\partial}_x\phi = \frac{1}{\kappa_x}\partial_x\phi + Q_x^\phi; \qquad \tilde{\partial}_z\phi = \frac{1}{\kappa_z}\partial_z\phi + Q_z^\phi, \tag{39}$$

where the memory variable is denoted $Q_{x,z}^\phi$. Memory variables obey a first-order in time differential equation for x-derivatives and z-derivatives. We will only give details for the $x-$derivative since it is similar for the z-derivatives. We consider the four time sub-steps $(t^{n,i})_{i=1,4}$ as $t^{n,i} = \Delta t(n+\nu_i)$ for the four RK4 stages where $\nu_i = 0$, $\nu_2 = 0.5$, $\nu_3 = 0.5$ and $\nu_4 = 1$. Then the memory variable Q_x^ϕ obey the following differential equation

$$Q_x^\phi\big(t^{n,i}\big) = b_{x,i}\, Q_z^\phi\big(t^{n,1}\big) + a_{x,i}\partial_x\phi\big(t^{n,i}\big), \tag{40}$$

where

$$a_{x,i} = -d_x\frac{\Delta t\nu_i}{\kappa_x\kappa_x(1+\Delta t\theta\nu_i(\frac{d_x}{\kappa_x}+b_x))}; \qquad b_x = \frac{\kappa_x - \theta\Delta t\nu_i(d_x+\kappa_x\alpha_x)}{\kappa_x+\theta\Delta t\nu_i(d_x+\kappa_x\alpha_x)}, \tag{41}$$

with

$$\begin{aligned}
\tau_x &= \frac{1}{\frac{d_x}{\kappa_x}+\alpha_x}; \qquad \kappa_x = 1 + (\kappa_{max}-1)^m;\\
d_x &= d_0\left(\frac{x}{L}\right)^N; \qquad \alpha_x = \alpha_{max}\left[1 - \left(\frac{x}{L}\right)^p\right],
\end{aligned} \tag{42}$$

where the θ parameter indicates if the computation is performed explicitly ($\theta = 0$), semi-implicitly ($\theta = 0.5$) or implicitly ($\theta = 1$). Here this parameter is taken as $\theta = 0.5$. Since we are mainly interested in damping acoustic waves (most of the waves reaching the boundary will be acoustic waves) we take the same parameters as in Martin et al. (2010), meaning that

$$\begin{aligned} N = 2; \qquad m = 2; \qquad p = 1; \qquad \alpha_{max} = \pi f_0; \\ \kappa_{max} = 7; \qquad d_0 = -\frac{(N+1)c_{max,x} log(R_c)}{2L}, \end{aligned} \tag{43}$$

where f_0 is the dominant frequency of the source, $c_{max,x}$ the maximum effective velocity along x (sum of background flow velocity and adiabatic sound speed) and R_c the theoretical reflection coefficient taken as $R_c = 0.0001$. The same formulation holds for derivatives along z.

Appendix 3: "Image" Boundary Conditions

This boundary condition consists in duplicating the physical domain and sources at ghost points located below the bottom boundary in order to obtain a wave interference ensuring zero vertical velocity at the boundary (Morse and Ingard 1968, Sect. 7.4). One enforces that the pressure is equal on each side of the boundary

$$p(-\mathbf{x}, t) = p(\mathbf{x}, t), \quad \forall \mathbf{x} \in \Omega \backslash \Gamma \tag{44}$$

and the sign of gravity and wind is changed in the ghost domain as

$$\begin{aligned} g_y(-\mathbf{x}) &= -g_y(\mathbf{x}), \\ w_x(-\mathbf{x}) &= -w_x(-\mathbf{x}), \quad \forall \mathbf{x} \in \Omega \backslash \Gamma. \end{aligned} \tag{45}$$

while all other unknowns are duplicated from the real domain to the ghost one

$$\begin{aligned} &\mu(-\mathbf{x}) = \mu(\mathbf{x}), \eta_V(-\mathbf{x}) = \eta_V(\mathbf{x}), \\ &\tau_\epsilon(-\mathbf{x}) = \tau_\epsilon(\mathbf{x}), \tau_\sigma(-\mathbf{x}) = \tau_\sigma(\mathbf{x}), \quad \forall \mathbf{x} \in \Omega \backslash \Gamma \end{aligned} \tag{46}$$

As a consequence, the pressure being equal on both sides of the boundary, the pressure gradient in the momentum equation is zero at the boundary. Also, setting opposite gravity directions above and below the boundary leads to zero gravity at the surface, hence the gravity term in the momentum equation vanishes. Therefore, at the boundary, the momentum equation is verified since the zero velocity condition is imposed. Finally, we impose the boundary to be motionless and we choose

$$\begin{aligned} v_x(x, -z) &= -v_x(x, z), \\ v_z(x, -z) &= -v_z(x, z), \quad \forall z \in \Omega. \end{aligned} \tag{47}$$

References

M. Abramowitz, I.A. Stegun, *Handbook of Mathematical Functions: with Formulas, Graphs, and Mathematical Tables*, vol. 55 (Courier Corporation, Hartford, 1964)

J. Artru, T. Farges, P. Lognonné, Acoustic waves generated from seismic surface waves: propagation properties determined from doppler sounding observation and normal-modes modeling. Geophys. J. Int. **158**, 1067–1077 (2004). doi:10.1111/j.1365-246X.2004.02377.x

J. Artru, V. Ducic, H. Kanamori, P. Lognonné, M. Murakami, Ionospheric detection of gravity waves induced by tsunamis. Geophys. J. Int. **160**, 840–848 (2005). doi:10.1111/j.1365-246X.2005.02552.x

W.B. Banerdt, S. Smrekar, P. Lognonné, T. Spohn, S.W. Asmar, D. Banfield, L. Boschi, U. Christensen, V. Dehant, W. Folkner, D. Giardini, W. Goetze, M. Golombek, M. Grott, T. Hudson, C. Johnson, G. Kargl, N. Kobayashi, J. Maki, D. Mimoun, A. Mocquet, P. Morgan, M. Panning, W.T. Pike, J. Tromp, T. van Zoest, R. Weber, M.A. Wieczorek, R. Garcia, K. Hurst, InSight: a discovery mission to explore the interior of Mars, in *Lunar and Planetary Science Conference*, vol. 44, 2013, p. 1915

D. Banfield, InSight Science Team, Atmospheric observations from the Mars insight mission, in *Mars Atmosphere: Modelling and Observation, 5th International Workshop*, ed. by F. Forget, M. Millour, 2014, p. 4304

H.E. Bass, J.P. Chambers, Absorption of sound in the Martian atmosphere. J. Acoust. Soc. Am. **109**, 3069–3071 (2001)

Q. Brissaud, R. Martin, R. Garcia, D. Komatitsch, Finite-difference numerical modelling of gravito-acoustic wave propagation in a windy and attenuating atmosphere. Geophys. J. Int. (2016). doi:10.1093/gji/ggw121

S.L. Bruinsma, J.M. Forbes, Medium- to large-scale density variability as observed by CHAMP. Space Weather **6**, 08002 (2008). doi:10.1029/2008SW000411

J.M. Carcione, *Wave Fields in Real Media: Wave Propagation in Anisotropic, Anelastic, Porous and Electromagnetic Media*, 2nd edn. (Elsevier, Oxford, 2007)

J.M. Carcione, D. Kosloff, R. Kosloff, Wave propagation simulation in a linear viscoelastic medium. Geophys. J. Int. **95**(3), 597–611 (1988)

J.E. Chappelow, V.L. Sharpton, Atmospheric variations and meteorite production on Mars. Icarus **184**, 424–435 (2006). doi:10.1016/j.icarus.2006.05.013

A. Colaïtis, A. Spiga, F. Hourdin, C. Rio, F. Forget, E. Millour, A thermal plume model for the Martian convective boundary layer. J. Geophys. Res., Planets **118**, 1468–1487 (2013). doi:10.1002/jgre.20104

C. de Groot-Hedlin, M.A.H. Hedlin, K. Walker, Finite difference synthesis of infrasound propagation through a windy, viscous atmosphere: application to a bolide explosion detected by seismic networks. Geophys. J. Int. **185**(1), 305–320 (2011). doi:10.1111/j.1365-246X.2010.04925.x

J.-X. Dessa, J. Virieux, S. Lambotte, Infrasound modeling in a spherical heterogeneous atmosphere. Geophys. Res. Lett. **32**, 12808 (2005). doi:10.1029/2005GL022867

F. Ding, W. Wan, H. Yuan, The influence of background winds and attenuation on the propagation of atmospheric gravity waves. J. Atmos. Sol.-Terr. Phys. **65**, 857–869 (2003). doi:10.1016/S1364-6826(03)00090-7

W.N. Edwards, Meteor generated infrasound: theory and observation, in *Infrasound Monitoring for Atmospheric Studies* (Springer, Amsterdam, 2010), pp. 361–414

F. Forget, F. Hourdin, R. Fournier, C. Hourdin, O. Talagrand, M. Collins, S.R. Lewis, P.L. Read, J.-P. Huot, Improved general circulation models of the Martian atmosphere from the surface to above 80 km. J. Geophys. Res. **104**, 24155–24176 (1999). doi:10.1029/1999JE001025

F. González-Galindo, F. Forget, M.A. López-Valverde, M. Angelats i Coll, E. Millour, A ground-to-exosphere Martian general circulation model, I: seasonal, diurnal, and solar cycle variation of thermospheric temperatures. J. Geophys. Res., Planets **114**, 04001 (2009). doi:10.1029/2008JE003246

W. Gropp, E. Lusk, A. Skjellum, *Using MPI, portable parallel programming with the Message-Passing Interface* (MIT Press, Cambridge, USA, 1994)

A.D. Hanford, L.N. Long, The direct simulation of acoustics on Earth, Mars, and Titan. J. Acoust. Soc. Am. **125**, 640 (2009). doi:10.1121/1.3050279

C.P. Haynes, C. Millet, A sensitivity analysis of meteoric infrasound. J. Geophys. Res., Planets **118**, 2073–2082 (2013). doi:10.1002/jgre.20116

C.O. Hines, Internal atmospheric gravity waves at ionospheric heights. Can. J. Phys. **38**, 1441 (1960). doi:10.1139/p60-150

D. Komatitsch, R. Martin, An unsplit convolutional perfectly matched layer improved at grazing incidence for the seismic wave equation. Geophysics **72**(5), 155–167 (2007)

S.R. Lewis, M. Collins, P.L. Read, F. Forget, F. Hourdin, R. Fournier, C. Hourdin, O. Talagrand, J.-P. Huot, A climate database for mars. J. Geophys. Res. **104**, 24177–24194 (1999). doi:10.1029/1999JE001024

J.Y. Liu, Y.B. Tsai, S.W. Chen, C.P. Lee, Y.C. Chen, H.Y. Yen, W.Y. Chang, C. Liu, Giant ionospheric disturbances excited by the M9.3 Sumatra earthquake of 26 December 2004. Geophys. Res. Lett. **33**, 2103 (2006). doi:10.1029/2005GL023963

R. Martin, D. Komatitsch, S.D. Gedney, E. Bruthiaux, A high-order time and space formulation of the unsplit perfectly matched layer for the seismic wave equation using auxiliary differential equations (ADE-PML). Comput. Model. Eng. Sci. **56**(1), 17 (2010). doi:10.3970/cmes.2010.056.017

B. Mikhailenko, A. Mikhailov, Numerical modeling of seismic and acoustic-gravity waves propagation in an Earth-atmosphere model in the presence of wind in the air. Numer. Anal. Appl. **7**(2), 124–135 (2014)

P.M. Morse, K.U. Ingard, *Theoretical Acoustics* (Princeton Univ. Press, New Jersey, 1968)

C.J. Nappo, *An Introduction to Atmospheric Gravity Waves* (Academic Press, Amsterdam, 2002), p. 276

V.E. Ostashev, D.K. Wilson, L. Liu, D.F. Aldridge, N.P. Symons, D. Marlin, Equations for finite-difference, time-domain simulation of sound propagation in moving inhomogeneous media and numerical implementation. J. Acoust. Soc. Am. **117**(2), 503–517 (2005). doi:10.1121/1.1841531

A. Petculescu, R.M. Lueptow, Atmospheric acoustics of Titan, Mars, Venus, and Earth. Icarus **186**, 413–419 (2007). doi:10.1016/j.icarus.2006.09.014

A.L. Pichon, K. Antier, Y. Cansi, B. Hernandez, E. Minaya, B. Burgoa, D. Drob, L.G. Evers, J. Vaubaillon, Evidence for a meteoritic origin of the September 15, 2007, Carancas crater. Meteorit. Planet. Sci. **43**, 1797–1809 (2008). doi:10.1111/j.1945-5100.2008.tb00644.x

O. Popova, I. Nemtchinov, W.K. Hartmann, Bolides in the present and past martian atmosphere and effects on cratering processes. Meteorit. Planet. Sci. **38**, 905–925 (2003). doi:10.1111/j.1945-5100.2003.tb00287.x

L.M. Rolland, G. Occhipinti, P. Lognonné, A. Loevenbruck, Ionospheric gravity waves detected offshore Hawaii after tsunamis. Geophys. Res. Lett. **37**, 17101 (2010). doi:10.1029/2010GL044479

G. Tancredi, J. Ishitsuka, P.H. Schultz, R.S. Harris, P. Brown, D.O. Revelle, K. Antier, A. Le Pichon, D. Rosales, E. Vidal, M.E. Varela, L. Sánchez, S. Benavente, J. Bojorquez, D. Cabezas, A. Dalmau, A meteorite crater on Earth formed on September 15, 2007: the Carancas hypervelocity impact. Meteorit. Planet. Sci. **44**, 1967–1984 (2009). doi:10.1111/j.1945-5100.2009.tb02006.x

J.D. Walker, Loading sources for seismological investigations of asteroids and comets. Int. J. Impact Eng. **29**, 757–769 (2003). doi:10.1016/j.ijimpeng.2003.10.022

F.J.W. Whipple, The great Siberian meteor and the waves, seismic and aerial, which it produced. Q. J. R. Meteorol. Soc. **56**, 287–304 (1930)

J.-P. Williams, Acoustic environment of the Martian surface. J. Geophys. Res. **106**, 5033–5042 (2001). doi:10.1029/1999JE001174

D.K. Wilson, L. Liu, Finite-difference, time-domain simulation of sound propagation in a dynamic atmosphere. Technical report, Cold Regions Research and Engineering Lab, Hanover Netherlands, 2004